Nanoscale

Check for updates

Continuous flow synthesis of plasmonic magnesium nanoparticles with tunable optical properties from grignard precursors

Vladimir Lomonosov, [ID] [a,b,c] Andrey Ten, [ID] [a,b] Bruno Pinho, [c] Zeki Semih Pehlivan, [a] Emilie Ringe [ID] [a,b] and Laura Torrente-Murciano [ID] *[c]

Nanoscale magnesium is an earth-abundant, inexpensive material that can efficiently utilize the energy of light *via* localized surface plasmon resonances. In this work, the continuous flow synthesis of plasmonic Mg nanoparticles with exquisite size control and high reaction yields is demonstrated thanks to the combination of fast mixing achieved in flow reactors and the use of highly reactive and air-sensitive Grignard precursors. The size distribution is controlled by tuning the mean residence time and adjusting the precursor concentration. A systematic study reveals that the reactivities of Grignard compounds toward reduction into plasmonic Mg are controlled by both electronic and steric factors defined by the structure of the organic substituent of the Grignard reagent. This work demonstrates the continuous, controllable, and tuneable manufacturing of plasmonic Mg nanoparticles with a great potential in light-harvesting applications.

Nanoparticles (NPs) of free-electron metals can sustain localized surface plasmon resonances (LSPRs), a collective oscillation of their delocalized electron cloud under incident light excitation. The resonant extinction cross-section of a plasmonic NP can exceed its physical cross-section, making it a nanoscale light antenna. Once absorbed, the energy captured from light to excite LSPRs decays through various pathways, ranging from electron–hole pair generation to heat production.[1–3] Such enhanced light–matter interaction renders plasmonic structures attractive for a variety of light-harvesting applications, including photocatalysis,[4–7] photothermal cancer therapy,[8,9] and surface-enhanced spectroscopies.[10,11] Mg is an earth-abundant plasmonic metal with dielectric properties that enable strong resonances across ultraviolet, visible and near-infrared wavelengths.[12–15] Excellent stability provided by a native self-limiting oxide layer,[16] as well as low price and biocompatibility[17,18] make Mg a real contender to well-established plasmonic metals such as Au, Ag, Cu, and Al. The potential of Mg NPs as an alternative plasmonic material for variety of applications has indeed recently been demonstrated.[19–26]

The LSPR frequency strongly depends on the size and shape of the plasmonic NP, and, therefore, controllable synthesis of Mg nanostructures is required for their efficient application. A previously reported colloidal synthesis of Mg NPs *via* one-step batch reduction of di-*n*-butylmagnesium (MgBu$_2$) with lithium naphthalenide radical anion complex results in Mg nanoplatelets with a broad average size distribution and optical response, which hinders their potential application.[27,28] The size distribution can be improved by utilizing a one-pot seed-mediated growth approach, which produces Mg nano spheroids with a narrow size distribution.[29,30] However, due to the relatively slow reduction rate of MgBu$_2$, Mg yields of only <30% can be achieved after several hours of reaction for both one- and two-step processes.[27,28,30] Grignard reagents with the general formula R-Mg-X (where X is a halogen and R is an organic group) are common reagents in organic synthesis and produced on an industrial scale. In contrast to MgBu$_2$, Grignard reagents are not pyrophoric, with simpler safety handling procedures. However, Mg NPs synthesis from Grignards reagents in batch reactors leads to micron-scale polycrystalline Mg particles within the first 5 minutes of reaction (Fig. S1).[28] The addition of a large excess of PVP capping ligand allows for improving NP morphology and reducing aggregation, however, the application of the resulting particles is hindered by their broad size distribution and lack of size control. The reported challenges in Mg NP synthesis from Grignard reagents are attributed to their high reactivity toward the reduction into Mg^0 with a relatively fast

[a]Department of Materials Science and Metallurgy, University of Cambridge, 27 Charles Babbage Road, Cambridge, UK, CB3 0FS, UK
[b]Department of Earth Sciences, University of Cambridge, Downing Street, Cambridge, UK, CB2 3EQ, UK
*[c]Department of Chemical Engineering and Biotechnology, University of Cambridge, Philippa Fawcett Drive, Cambridge CB3 0AS, UK. E-mail: lt416@cam.ac.uk*

reaction time with respect to the slow mixing time, leading to heterogeneous conditions at early reaction times.

Efficient mass transport to ensure rapid mixing during early reaction stages and during the synthesis can be achieved by tailored design of flow systems. Our group has demonstrated the influence of mixer configurations for the rapid mixing of reactants.[31] In addition, 3D reactor configurations such as helical or coiled inverter reactors can modify the fluid dynamics of the system, leading to narrow residence time distributions (in contrast to those characteristic of laminar flow) to produce uniform metal NPs in the absence of capping agents.[32–35] A range of strategies have been developed to manipulate the fluid dynamics of flow reactors for the synthesis of a wide range of materials.[36–38] More recently, we have demonstrated the intrinsically safer nature of flow microreactors for stable and safe organometallic reactions in bi-phasic systems.[39]

In this work, the colloidal synthesis of plasmonic Mg NPs in continuous flow reactors is carried out under ambient conditions in tetrahydrofuran (THF). Fast and efficient mixing in continuous flow helical reactors enables the use of highly reactive Grignard reagents as Mg precursors under homogeneous reaction conditions, resulting in Mg NPs with narrow size distributions and tunable optical properties. Their size distribution can be controlled by changing the mean residence time and adjusting the precursor concentration. Importantly, both reaction rates and Mg NPs size/morphology are also largely dependent on the composition of the Grignard reagent. A systematic study of the relationship between the Grignard organic group and its reactivity toward Mg reduction reveals that the reaction kinetics is affected by electronic and steric factors. As a result, the synthesis of tailored Mg NPs can be achieved thanks to the variety of commercially available Grignard compounds.

Herein, Mg NPs are synthesized in flow microreactors using a range of Grignard reagents as Mg precursors, and a Li-phenanthrene (LiPhen) radical anion complex as reducing agent (1):

$$R\text{-}Mg\text{-}X + 2Li^+ \left[\right]^{\bullet -} \longrightarrow Mg^0 + Li\text{-}X + Li\text{-}R \quad (1)$$
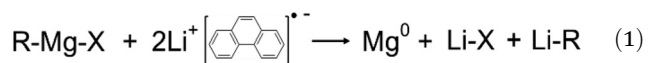
In a typical experiment, 0.1 M solution of the Grignard reagent and 0.25 M solution of freshly prepared LiPhen both in THF are continuously co-fed and mixed at equal flowrates in a T-mixer (internal diameter, i.d. = 0.5 mm), and a the resulting mixture is fed into a glass helical reactor (i.d. = 1.5 mm, length L = 3.2 m, helical diameter = 10 mm) to produce Mg NPs at room temperature. The reactor outlet stream is continuously mixed with iso-propanol (IPA) or acetone in another T-mixer to quench unreacted Mg precursor and reducing agent and stop the reaction (Fig. 1a). Note that 0.5 mg mL^{-1} of polyvinylpyrrolidone (PVP) with M_w = 10 000 is added to the reducing agent solution to act as a capping agent during the Mg NPs synthesis.[28] To remove the residual by-products, the samples are cleaned by centrifugation and redispersion steps
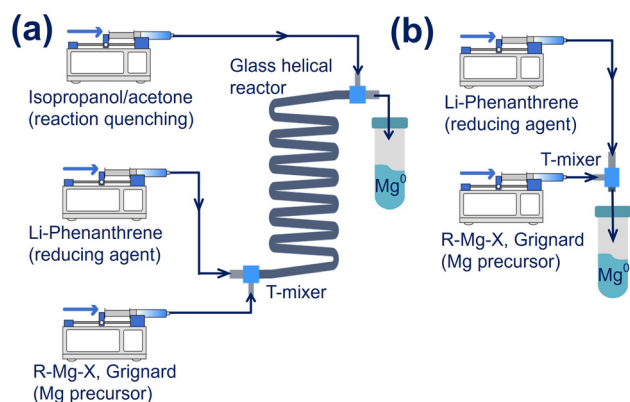

Fig. 1 Continuous flow synthesis reactor setups: syringe pumps control the flowrates of Grignard reagent (R-Mg-X, Mg precursor), LiPhen radical anion complex (reducing agent), and IPA or acetone (reaction quenching). Reactants are mixed in a T-mixer and (a) pass through the glass helical reactor (i.d. = 1.5 mm, L = 0.65, 2.0, 3.2 m, helical diameter = 10 mm). Unreacted Mg precursor and reducing agent are quenched in a T-mixer with a flow of IPA or acetone at the reactor outlet; (b) reaction products are collected directly at the T-mixer outlet into a 2 mL microcentrifuge tube containing 1 mL of IPA.

in anhydrous acetone, THF, and twice in IPA. Detailed experimental protocols and NP characterization procedures can be found in the SI.

The effect of the Grignard reagent organic group on the resulting properties of Mg NPs is investigated in a continuous flow synthesis using a 3.2 m long helical reactor with constant flowrates corresponding to a mean residence time of 170 s (Fig. 1a). Optical properties, morphology, and average size distributions of Mg NPs are affected by the structure of the organic group in the Grignard reagent (Fig. 2). Roughly spherical NPs with randomly distributed flat and angled facets across their surface are produced from methyl-, *n*-butyl-, and phenyl-MgCl precursors, whereas hexagonal nanoplatelets are formed from *t*-butyl-MgCl (Fig. 2). The spheroidal NPs are characterised with narrow size distributions and extinction maxima in the visible range, while nanoplatelets demonstrate a broad size distribution and extinction in the near-IR region. The formation of nanoplates from *t*-butyl-MgCl can indicate slower nucleation and growth leading to a closer to thermodynamic hexagonal shape, previously observed for the less reactive MgBu$_2$ precursor,[27,30] while spheroidal NPs are produced *via* fast, kinetically controlled growth. Note, the broadening in the LSPR peak of the Mg NPs produced from methyl- and butyl-MgCl compared to those obtained from phenyl-MgCl can be explained by an enhanced partial NP aggregation in the colloid due to their smaller size and lower degree of interaction with bulky PVP molecules. The difference in size and shape of Mg NPs produced from the different Grignard reagents is attributed to their different reactivities toward reduction into Mg^0, which affect nucleation and growth rates. Indeed, the reduction of methyl-, *n*-butyl-, and phenyl-MgCl leads to Mg yields of 57, 49, and 45%, respectively, whereas
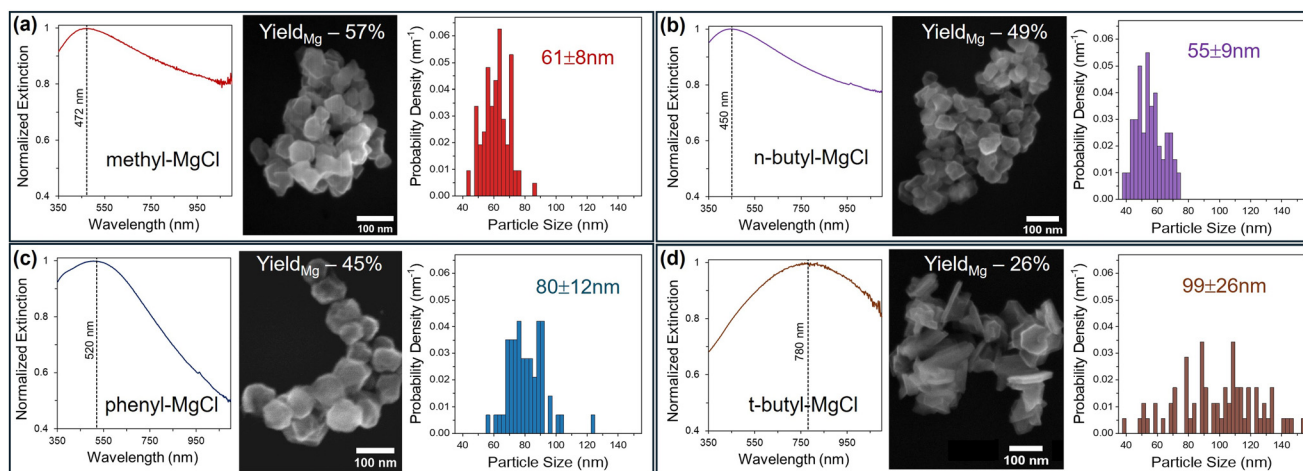
Fig. 2 Continuous synthesis of Mg NPs from Grignard reagents with different organic groups. UV-Vis-NIR extinction spectra, representative SEM images, Mg yields, and size distribution diagrams for Mg NPs produced from (a) methyl-MgCl; (b) *n*-butyl-MgCl; (c) phenyl-MgCl; and (d) *t*-butyl-MgCl. Solutions of Grignard reagent and LiPhen (in the presence of PVP) are mixed in a T-mixer and co-fed into a 3.2 m long helical reactor at total flow rate of 2 mL min^{-1} with a 170 s residence time (shown in Fig. 1a).

Table 1 Effect of organic substituent of the Grignard reagent on the yield of Mg as a function of residence time. A residence time of <1 s was achieved using the reaction setup depicted in Fig. 1b (mixer, no reactor). A residence time of 170 s was achieved using the reaction setup depicted in Fig. 1a with a 3.2 m long helical reactor and a total flowrate of 2 mL min^{-1}

Grignard reagent/ residence time	Methyl-MgCl Mg yield, %	*n*-Butyl-MgCl	iso-butyl-MgCl	2-Methylallyl-MgCl	Benzyl-MgCl	Phenyl-MgCl	*t*-Butyl-MgCl
<1 s	53	45	42	51	41	0	0
170 s	57	49	—	—	—	45	26

only 26% yield is achieved when using *t*-butyl-MgCl, all after 170 s of reaction (Table 1). The Mg yield is calculated as:

$$\text{Yield}_{\text{Mg}} = \frac{\text{Mg}_{\text{out}}}{\text{Mg}_{\text{in}}} \times 100\%, \quad (2)$$

where Mg_{in} and Mg_{out} are Mg molar concentrations in the initial reaction mixture and in the extracted solid product (based on inductively coupled plasma optical emission spectrometry (ICP-OES) data, see SI for details).

To provide insights on the differences in reactivities of the Grignard Mg precursors, the same reactions were carried out but quenched immediately after the initial T-mixer (Fig. 1b), enabling the calculation of Mg yields at early reaction times. In this configuration, the mean residence is estimated to be <1 s. The initial Mg yield at <1 s depends dramatically on the structure of the organic substituent of the Grignard reagent: no product is detected when phenyl- and *t*-butyl-MgCl are used, whereas methyl- and *n*-butyl-MgCl produce high reaction yields (Table 1) comparable to those achieved after 170 s.

These results reveal the importance of the steric and electronic properties of the organic group on the reactivity of Grignard precursors for Mg NPs synthesis based on the following mechanistic considerations. As shown in reaction (3), reduction of Grignard reagents into Mg metal requires the transfer of 2 electrons to Mg^{2+} from the LiPhen radical-anion

complex and the cleavage of the Mg–carbon and Mg–halogen bonds. The cleavage of the ionic Mg–halogen bond leads to the formation of a stable lithium halide salt and should be favourable in polar solvent (THF). On the other hand, the relative electronegativities of carbon and Mg suggest a polar nature of the C–Mg bond with the bonding pair of electrons pulled toward the carbon atom. The heterolytic splitting of the C–Mg bond generates a transition state with the formation of a highly unstable carbanion R$^-$ and, therefore, it can be assumed to be the rate limiting step. One should note that despite the polar nature of the C–Mg bond in the Grignard reagent, homolytic splitting leading to the formation of an unstable radical R$^{\bullet}$ cannot be completely ruled out.
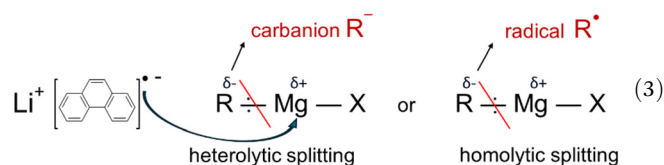
Stabilization of the electron-rich carbanion requires an electron-withdrawing group, whereas the electron-deficient radical needs electron donation. Our experimental results demonstrate that the reactivity of Grignard reagents decreases with increasing electron donating properties of the alkyl substituent: methyl > *n*-butyl > *t*-butyl (Table 1), indicating heterolytic

splitting of the Mg–R bond. Note, the low reactivity of phenyl-MgCl precursor observed here correlates well with a low stability of the phenyl-carbanion, in which the lone pair on the benzene is in the plane of the ring and hence cannot interact with the conjugated π-system.

The important role of the electronic properties of the organic group in the reactivity of Grignard reagents is further confirmed by experiments performed with benzyl-MgCl and 2-methylallyl-MgCl. Both of these precursors show high reactivity due to their ability to produce relatively stable carbanions, in which the electron density is delocalized *via* resonance effects. Furthermore, the reactivity of 2-methylallyl-MgCl can be compared to that of iso-butyl-MgCl, which has the same structure but without π-bonds, and, therefore, lacks resonance stabilization. The yield at ~1 s produced from iso-butyl-MgCl (42%) is indeed noticeably lower compared to 2-methylallyl-MgCl (51%) (Table 1). Similarly, the Mg yield at ~1 s achieved with iso-butyl-MgCl (42%) is slightly lower than that obtained for *n*-butyl-MgCl (45%), which also correlates well with the electron donating ability of these organic groups.

The results in Table 1 also demonstrate that along with electronic effects, the reactivities of Grignard reagents toward reduction into Mg^0 are also affected by steric factors. The Mg yield at ~1 s obtained using 2-methylallyl-MgCl (51%) is similar to that obtained with the less stable methyl-MgCl (53%), and drops to 41% when the resonance-stabilized benzyl-MgCl is used as Mg precursor. These observations reveal that despite the ability of 2-methylallyl-MgCl and benzyl-MgCl precursors to produce a carbanion of higher stability compared to methyl-MgCl, the reactivities of these compounds are hindered by steric factors.

The high reactivity of Grignard reagents toward reduction into Mg^0 allows continuous synthesis of Mg NPs with high reaction yields at low residence times of <1 s. However, such high reaction rates imply that the reaction proceeds under non-homogeneous mixing of the Mg precursor and reducing agent. As a consequence of the mixing time being longer than the reaction time, nucleation and growth of NPs take place at different rates in different fluid elements, resulting in broad size distributions. To understand this effect deeper, the effect of residence time on Mg yield was studied by varying the flowrates in a 3.2 m long helical reactor (Table 2). Highly reactive methyl-MgCl and *n*-butyl-MgCl precursors show a small increase in Mg yield as a function of residence time (Table 2), with most of the conversion achieved within ~1 s of the reaction as discussed above, leading to spheroidal NPs; no change

in their UV-Vis-NIR extinction was observed as function of residence time (Fig. S2). In contrast, for the least reactive Grignard reagent, *t*-butyl-MgCl which contains both bulky and electron donating group, the reaction yield progressively increases with residence time from 8% at 55 s to 26% at 170 s (Table 2). In this case, the mixing time is shorter than the reaction time and the reaction takes place under homogeneous conditions. However, such low reactivity leads to large, close to thermodynamic shape hexagonal platelets (Fig. 2d) with a broad size distribution.

A compromise in reactivity is achieved with phenyl-MgCl precursor where the Mg yield increases progressively with residence time, leading to kinetic faceted spheroidal NPs (Fig. 2c and S3). The size of the particles can be finely tuned by varying the residence time (Fig. 3a). As expected, the increase in size is accompanied by a red shift in extinction (Fig. 3b) and its accompanying change in colour of the NP colloids (Fig. 3c). The extinction profile of Mg NPs can be further tuned by increasing the amount of Mg precursor in the reaction mixture: a 2-fold increase (from 0.1 M to 0.2 M) in the phenyl-MgCl concentration leads to a redshift of the extinction maximum (Fig. 3b). The fact that the increase in precursor concentration boosts Mg yield to up to 56% (Table S1) indicates an increase in the reduction rates. Note, both NP size and reaction yield can be potentially further increased by increasing the concentration of the LiPhen reducing agent. However, our results demonstrate that a higher phenanthrene concentration leads to a noticeable increase in the viscosity of the reducing agent solution and higher pressure drop along the reactor, affecting flow stability. Furthermore, the excess of the reducing agent leads to a substantial contamination of Mg NPs with additional phenanthrene released upon the reaction quenching and requires extra cleaning steps.

The metallic character of the Mg NPs is confirmed by scanning transmission electron microscopy electron energy loss spectroscopy (STEM-EELS), where Mg^0 is revealed by its unique bulk plasmon signal (Fig. 3d and e). The presence of Mg^0 as the main phase is further supported by powder XRD analysis (Fig. 3f). Particularly, the XRD pattern reveals peaks corresponding to Mg's hexagonal close-packed crystal structure (JCPDS 04-0770) with no MgO (JCPDS 89-7746) peaks detected, indicating that the oxide shell has a small domain size, consistent with a polycrystalline, sub-10 nm shell for Mg NPs as previously reported.[14]

As the flowrate in microreactors affects the fluid dynamics of the system, to decouple its impact from that of the residence

Table 2 Effects of flow rate and residence time on Mg yield synthesised in a 3.2 m long continuous flow helical reactor with different Grignard reagents

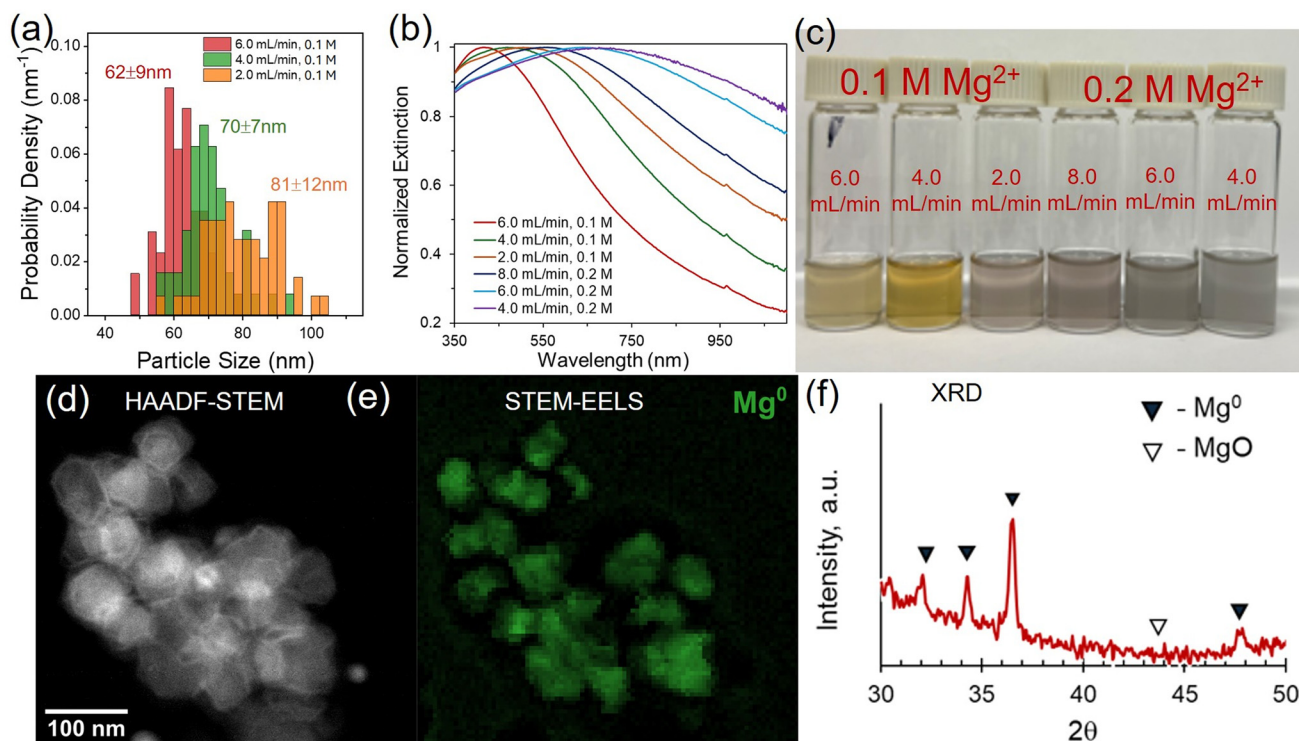| Flow rate, mL min^{-1}	Residence time, s	Methyl-MgCl Mg yield, %	*n*-Butyl-MgCl	Phenyl-MgCl	*t*-Butyl-MgCl
2	170	57	49	45	26
4	85	53	47	35	11
6	55	48	41	25	8

Fig. 3 Synthesis of Mg NPs from phenyl-MgCl precursor in a 3.2 m long flow microreactor. (a) Size distribution histograms, (b) UV-Vis–NIR extinction spectra, and (c) different colours of the resulting Mg NPs as a function of residence time and precursor concentration; (d) high-angle annular dark field (HAADF)-STEM image; (e) Mg bulk plasmon (~10.5 eV) map from STEM-EELS indicating the distribution of Mg^0 (green); (f) powder XRD patterns of Mg NPs produced at 2 mL min^{-1} and 170 s residence time.

time, a range of Mg NP syntheses was performed under constant conditions using phenyl-MgCl as the Mg precursor. In this case, the residence times were kept constant (55, 85, and 170 s) by simultaneously varying the length of the helical reactor (0.65, 2.0, and 3.2 m) and flow rate. Fig. 4a–c demonstrates that as residence time decreases, the extinction spectra of the resulting Mg NPs narrow and blueshift, revealing an effect of flow rate on fluid dynamics (*i.e.*, mixing of the Mg precursor and reducing agent streams) on the final product. To understand this phenomenon, fluid dynamic simulations of the system were carried out using Ansys Fluent 2023 R2 to study diffusion in the THF solvent (see SI for details). For this, a tracer was defined with the same properties than THF. A representative distribution of the tracer concentration along the reactor is depicted in Fig. 4e. In all cases, the fluid is under laminar flow with Reynolds numbers < 200. However, the helical reactor configuration promotes the formation of Dean vortices, leading to the rotation of the fluid from the centre of the reactor toward the walls, enhancing the rate of mixing of reactants.[40] The magnitude of this rotation is quantified by the dimensionless Dean number, defined as De = Re $(d/D)^{0.5}$ as a result of the balance of inertial, centrifugal, and viscous forces of a fluid flowing in a coiled channel, where d is the diameter of the reactor and D is its helical diameter, both kept constant in this study. The values of Dean and Reynolds numbers in all the experiments are presented in Table S2.

Fig. 4d shows the evolution of the mixing index along the length of the reactor as a function of flow rate (for the considered reactor configuration).[41] Mixing indices have values between 0 and 1, where 0 indicates two completely segregated streams and 1, perfectly mixed streams. One should note the logarithmic scale in the *x*-axis. Combining the experimental and simulation data in Fig. 4 reveals the importance of rapid mixing to enable homogenous nucleation in the early stages of the Mg synthesis. A threshold of De > 20–30 (corresponding here to a flowrate of 2 mL min^{-1}) is needed to achieve perfect mixing within the first few seconds of the reaction, resulting in narrow extinction spectra. Lower Dean numbers lead to the mixing of reactants being dominated by slow diffusion under laminar flow, resulting in broad and redshifted extinction.

Microscopic images of the Mg NPs produced in flow using Grignard reagents (Fig. 2 and 3d) include aggregates despite the presence of PVP as a capping agent. However, the pronounced maxima in the extinction spectra of the colloidal samples (Fig. 2 and 3b) as well as the visually observed colours of the Mg NPs colloids (Fig. 3c) suggest that the aggregation is, at least in part, due to drying artifacts. While for some applications, such as surface-enhanced Raman spectroscopy and plasmon-enhanced catalysis, aggregates can be beneficial due to the formation of highly localized regions of intense local field (electromagnetic hot spots), in most cases uncontrollable aggregation is considered undesirable. The dispersion of the
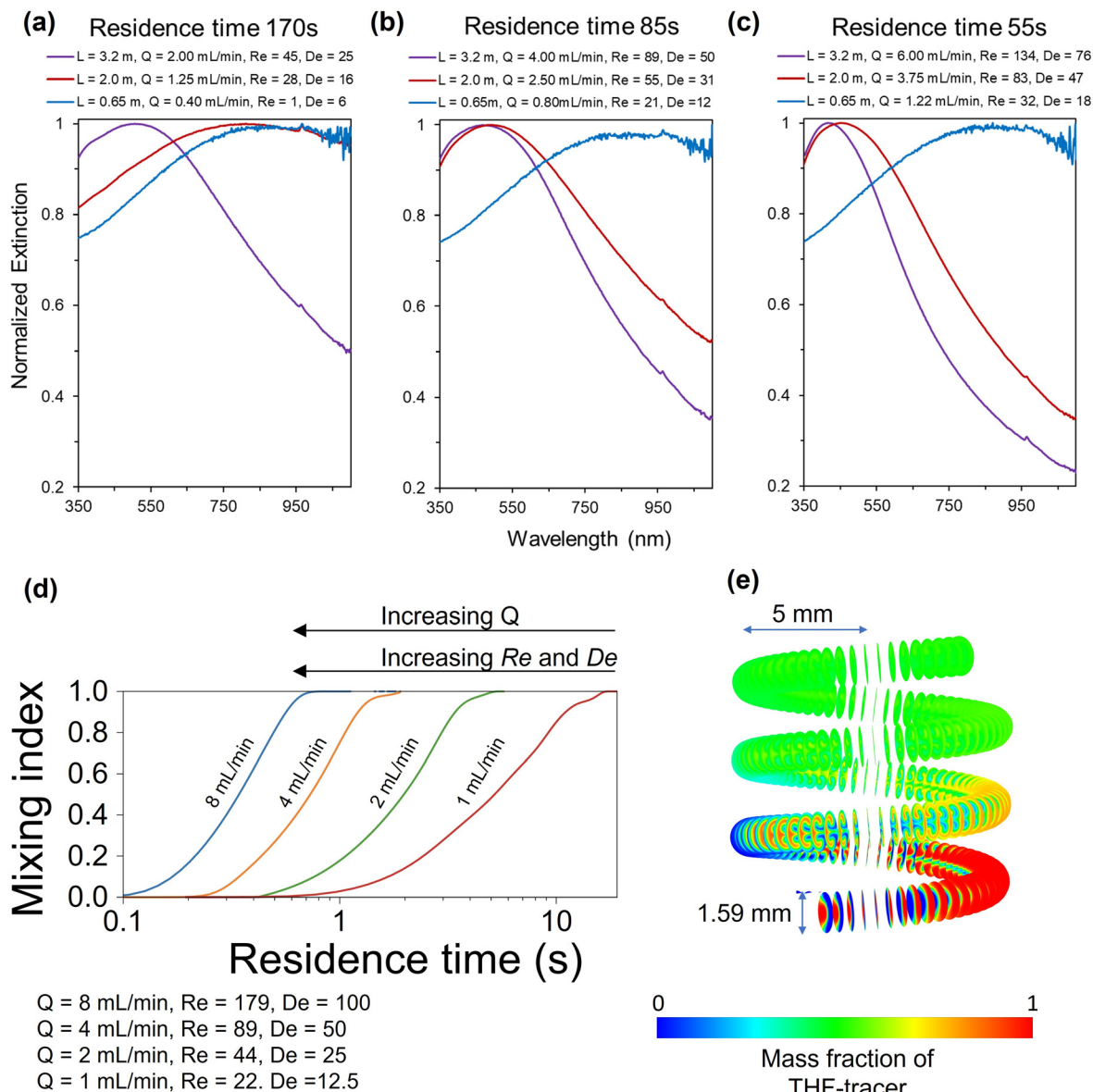
Fig. 4 Effect of fluid dynamics parameters on Mg NPs synthesised by continuous flow reduction of phenyl-MgCl. (a)–(c) UV-Vis–NIR extinction spectra of the Mg NPs at constant residence times (55, 85, and 170 s) obtained by simultaneously varying the length of the reactor and the total flow rate; (d) simulation of the evolution of the mixing index in the helical reactor at different flow rates; (e) representative distribution of the tracer concentration along the helical reactor at a 2 mL min^{-1} flow rate.

Mg NPs can be substantially improved by replacing IPA by acetone as the quenching solvent. As can be seen in Fig. 5, the Mg NPs produced in flow using phenyl-MgCl precursor and quenched with acetone are characterized by a sharper extinction profile (Fig. 5a) as well as high NP dispersion observed in SEM imaging (Fig. 5c and S4). The difference may be attributed to the potential for IPA to react with Mg metal and form magnesium isopropoxide, which potentially reduces the ability of the resulting NPs to interact with the PVP capping agent leading to higher aggregation.

While these results confirm that PVP acts as a capping agent to produce well-dispersed, colloidally stable Mg NPs, its presence can affect their final application by forming physical and electronic barriers as well as limiting the possibilities for further functionalization of the NP surface. When the flow synthesis of Mg NPs using phenyl-MgCl is carried out in the absence of PVP, the morphology of the resulting NPs changes dramatically, forming nanostars (Fig. 5). As before, their optical properties can be controlled by varying the mixing of the reactants (*i.e.*, varying flow rates, Fig. 5a), however, the assessment of their size distribution is difficult due to a high level of aggregation observed in SEM images (Fig. 5e). The extinction profiles of the Mg nanostars indicate the presence of plasmonic Mg^0 phase, however, their further
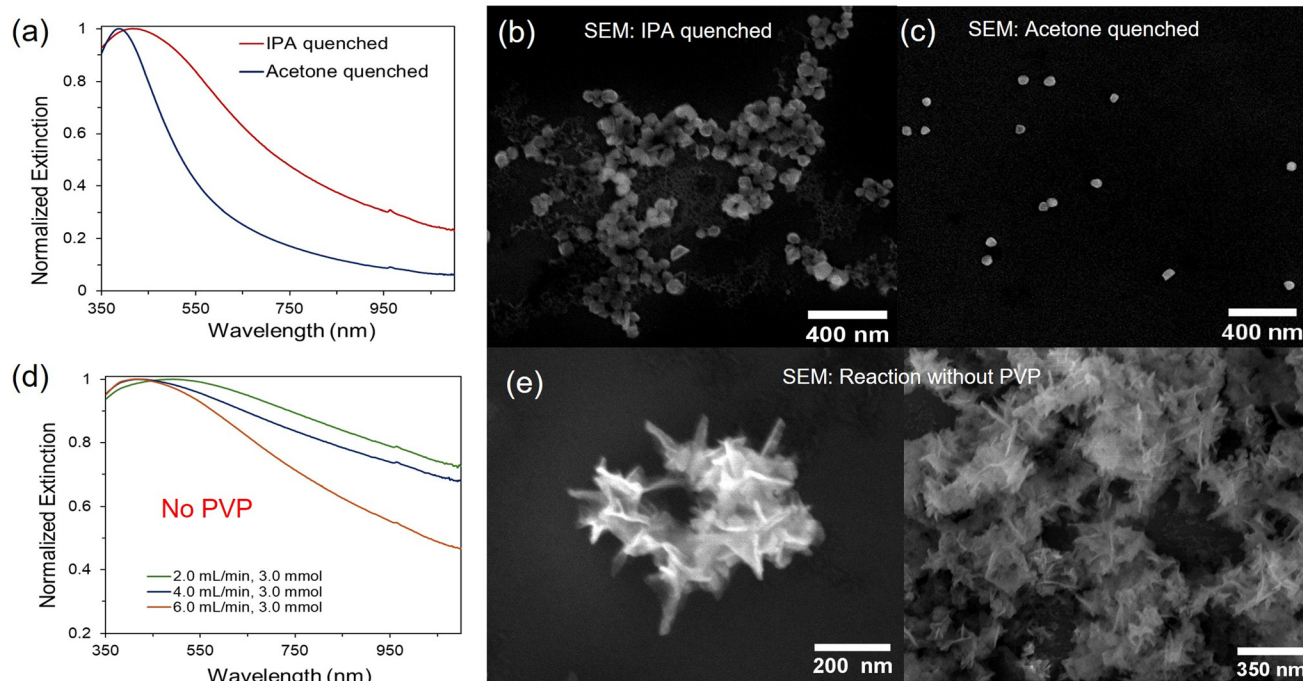
Fig. 5 Effects of capping agent and quenching solvent on the continuous synthesis of Mg NPs from phenyl-MgCl in a 3.2 m long reactor. (a) UV-Vis-NIR extinction spectra of Mg NPs quenched in IPA and acetone; (b) and (c) representative SEM images of Mg NPs produced at 2 mL min^{-1} and 170 s residence time quenched in IPA and acetone; (d) UV-Vis-NIR extinction spectra of Mg NPs produced without PVP at different residence times; (e) representative SEM images of Mg NPs produced without PVP at 2 mL min^{-1} and 170 s residence time.

characterisation is beyond the scope of the present study. These results reveal the important role of PVP as a shape-directing agent during flow synthesis of Mg NPs from Grignard reagents.

In conclusion, our results demonstrate that residence time control and fluid dynamics manipulation in helical flow microreactors enable the tunable continuous synthesis of Mg NPs by the reduction of Grignard Mg precursors with lithium phenanthrene as the reducing agent. The important role of steric and electronic properties of the organic group on the reactivity of Grignard reagents for their reduction into Mg NPs is shown. For the most reactive Grignard precursors, the reaction rate substantially exceeds the mixing time, leading to kinetic spheroidal NPs. However, for this series of precursors, heterogeneous nucleation conditions limit control over the NP size distribution. On the other hand, Grignard reagents with lower reactivities produce thermodynamic hexagonal nanoplatelets, similar to that obtained in colloidal batch synthesis with MgBu$_2$. A compromise between reactivity and mixing is found with phenyl-MgCl, where the rate of mixing allows to manipulate the size distribution and optical properties of the resulting Mg NPs.

Conflicts of interest

The authors declare no competing financial interest.

Data availability

The data supporting this article have been included as part of the supplementary information (SI). Supplementary information: details of continuous Mg NPs synthesis, UV-Vis-NIR spectra, XRD, SEM, HAADF-STEM and STEM-EELS analysis. Additional SEM images, UV-Vis-NIR extinction spectra, and yield data. See DOI: https://doi.org/10.1039/d5nr03384e.

Acknowledgements

Author contributions

The manuscript was written through the contribution of all authors.

References

1 E. Cortés, W. Xie, J. Cambiasso, A. S. Jermyn, R. Sundararaman, P. Narang, S. Schlücker and S. A. Maier, *Nat. Commun.*, 2017, **8**, 14880.

2 M. L. Brongersma, N. J. Halas and P. Nordlander, *Nat. Nanotechnol.*, 2015, **10**, 25–34.

3 G. V. Hartland, *Chem. Rev.*, 2011, **111**, 3858–3887.

4 C. Zhan, M. Moskovits and Z.-Q. Tian, *Matter*, 2020, **3**, 42–56.

5 S. Mukherjee, F. Libisch, N. Large, O. Neumann, L. V. Brown, J. Cheng, J. B. Lassiter, E. A. Carter, P. Nordlander and N. J. Halas, *Nano Lett.*, 2013, **13**, 240–247.

6 D. F. Swearer, H. Zhao, L. Zhou, C. Zhang, H. Robatjazi, J. M. P. Martirez, C. M. Krauter, S. Yazdi, M. J. McClain, E. Ringe, E. A. Carter, P. Nordlander and N. J. Halas, *Proc. Natl. Acad. Sci. U. S. A.*, 2016, **113**, 8916–8920.

7 P. Christopher, H. Xin and S. Linic, *Nat. Chem.*, 2011, **3**, 467–472.

8 X. Huang and M. A. El-Sayed, *Alexandria J. Med.*, 2011, **47**, 1–9.

9 D. Jaque, L. Martínez Maestro, B. del Rosal, P. Haro-Gonzalez, A. Benayas, J. L. Plaza, E. Martín Rodríguez and J. García Solé, *Nanoscale*, 2014, **6**, 9494–9530.

10 J. Langer, D. Jimenez de Aberasturi, J. Aizpurua, R. A. Alvarez-Puebla, B. Auguié, J. J. Baumberg, G. C. Bazan, S. E. J. Bell, A. Boisen, A. G. Brolo, J. Choo, D. Cialla-May, V. Deckert, L. Fabris, K. Faulds, F. J, G. d. Abajo, R. Goodacre, D. Graham, A. J. Haes, C. L. Haynes, C. Huck, T. Itoh, M. Käll, J. Kneipp, N. A. Kotov, H. Kuang, E. C. Le Ru, H. K. Lee, J.-F. Li, X. Y. Ling, S. A. Maier, T. Mayerhöfer, M. Moskovits, K. Murakoshi, J.-M. Nam, S. Nie, Y. Ozaki, I. Pastoriza-Santos, J. Perez-Juste, J. Popp, A. Pucci, S. Reich, B. Ren, G. C. Schatz, T. Shegai, S. Schlücker, L.-L. Tay, K. G. Thomas, Z.-Q. Tian, R. P. Van Duyne, T. Vo-Dinh, Y. Wang, K. A. Willets, C. Xu, H. Xu, Y. Xu, Y. S. Yamamoto, B. Zhao and L. M. Liz-Marzán, *ACS Nano*, 2020, **14**, 28–117.

11 E. Fort and S. Grésillon, *J. Phys. D: Appl. Phys.*, 2008, **41**, 013001.

12 T. G. Farinha, C. Gong, Z. A. Benson and M. S. Leite, *ACS Photonics*, 2019, **6**, 272–278.

13 J. S. Biggins, S. Yazdi and E. Ringe, *Nano Lett.*, 2018, **18**, 3752–3758.

14 E. Ringe, *J. Phys. Chem. C*, 2020, **124**, 15665–15679.

15 E. R. Hopper, C. Boukouvala, J. Asselin, J. S. Biggins and E. Ringe, *J. Phys. Chem. C*, 2022, **126**, 10630–10643.

16 V. Lomonosov, J. Yang, Y. Fan, S. Hofmann and E. Ringe, *Nano Lett.*, 2024, **24**, 7084–7090.

17 W. Zhou, Y. Zhang, S. Meng, C. Xing, M. Ma, Z. Liu, C. Yang and T. Kong, *Small Methods*, 2020, **5**(2), 202000920.

18 R. C. Martin, E. Locatelli, Y. Li, P. Matteini, I. Monaco, G. Cui, S. Li, M. Banchelli, R. Pini and M. Comes Franchini, *J. Mater. Chem. B*, 2016, **4**, 207–211.

19 V. Lomonosov, T. M. R. Wayman, E. R. Hopper, Y. P. Ivanov, G. Divitini and E. Ringe, *Nanoscale*, 2023, **15**, 7420–7429.

20 A. Ten, V. Lomonosov, C. Boukouvala and E. Ringe, *ACS Nano*, 2024, **18**, 18785–18799.

21 S. J. Patil, V. Lomonosov, E. Ringe and D. Kurouski, *J. Phys. Chem. C*, 2023, **127**, 7702–7706.

22 C. A. West, V. Lomonosov, Z. S. Pehlivan and E. Ringe, *Nano Lett.*, 2023, **23**, 10964–10970.

23 J. M. Sanz, D. Ortiz, R. Alcaraz de la Osa, J. M. Saiz, F. González, A. S. Brown, M. Losurdo, H. O. Everitt and F. Moreno, *J. Phys. Chem. C*, 2013, **117**, 19606–19615.

24 F. Sterl, N. Strohfeldt, R. Walter, R. Griessen, A. Tittl and H. Giessen, *Nano Lett.*, 2015, **15**, 7949–7955.

25 X. Duan, S. Kamin and N. Liu, *Nat. Commun.*, 2017, **8**, 14606.

26 T. Gong, P. Lyu and M. S. Leite, *ACS Appl. Opt. Mater.*, 2023, **1**, 825–831.

27 E. R. Hopper, T. M. R. Wayman, J. Asselin, B. Pinho, C. Boukouvala, L. Torrente-Murciano and E. Ringe, *J. Phys. Chem. C*, 2022, **126**, 563–577.

28 T. M. R. Wayman, V. Lomonosov and E. Ringe, *J. Phys. Chem. C*, 2024, **128**, 4666–4676.

29 A. Ten, C. Boukouvala, V. Lomonosov and E. Ringe, *Nanoscale Horiz.*, 2025, **10**, 1724–1730.

30 V. Lomonosov, E. R. Hopper and E. Ringe, *Chem. Commun.*, 2023, **59**, 5603–5606.

31 Y. Gao, D. F. Zhu, Y. Han and L. Torrente-Murciano, *J. Flow Chem.*, 2021, **11**, 589–598.

32 B. Pinho, L. M. Williams, J. Mahin, Y. Gao and L. Torrente-Murciano, *Chem. Eng. J.*, 2023, **471**, 144342.

33 K.-J. Wu and L. Torrente-Murciano, *React. Chem. Eng.*, 2018, **3**, 267–276.

34 K.-J. Wu, G. M. De Varine Bohan and L. Torrente-Murciano, *React. Chem. Eng.*, 2017, **2**, 116–128.

35 B. Pinho and L. Torrente-Murciano, *Adv. Energy Mater.*, 2021, **11**(32), 2100918.

36 Y. Gao, B. Pinho and L. Torrente-Murciano, *Curr. Opin. Chem. Eng.*, 2020, **29**, 26–33.

37 K. Zhang, Y. Gao, B. Pinho, R. L. Z. Hoye, S. D. Stranks and L. Torrente-Murciano, *Chem. Eng. J.*, 2023, **451**, 138752.

38 A. J. Exposito, P. J. Barrie and L. Torrente-Murciano, *ACS Sustainable Chem. Eng.*, 2020, **8**, 18297–18302.

39 F. F. Mulks, B. Pinho, A. W. J. Platten, M. R. Andalibi, A. J. Expósito, K. J. Edler, E. Hevia and L. Torrente-Murciano, *Chem*, 2022, **8**, 3382–3394.

40 K.-J. Wu and L. Torrente-Murciano, *React. Chem. Eng.*, 2018, **3**, 267–276.

41 Y. Gao, B. Pinho and L. Torrente-Murciano, *Chem. Eng. J.*, 2022, **432**, 134112.